Journal of Non-Newtonian Fluid Mechanics 309 (2022) 104918

Contents lists available at ScienceDirect

Journal of Non-Newtonian Fluid Mechanics

journal homepage: www.elsevier.com/locate/jnnfm

Scaling law for the viscoelasticity-induced particle migration in stirred vessels

Giovanni Meridiano, Weheliye Hashi Weheliye, Luca Mazzei *, Panagiota Angeli *

ThAMeS Multiphase, Department of Chemical Engineering, University College London, Torrington Place, London WC1E 7JE, United Kingdom

A B S T R A C T

In this study, we investigate the viscoelasticity-induced migration of solid particles immerged in the three-dimensional flow field created by the rotation of a Rushton turbine. At the same time, we propose a scaling law for predicting the characteristic particle migration time as a function of the Weissenberg number. Particle image velocimetry is adopted to reconstruct the three-dimensional velocity and deformation rate fields generated by the rotation of the Rushton turbine in both Newtonian and viscoelastic fluids; concurrently, particle tracking is used to measure the evolution of the particle distribution in the tank. The experimental campaign shows that the deformation rate field is essentially bi-dimensional and confined to the r-θ plane. Accordingly, the particles migrate only in the radial direction driven by the presence of gradients of shear rate on the r-θ plane. Finally, the scaling law is validated against experimental data obtained at different Weissenberg numbers, impeller diameters and fluid compositions. The results show good agreement between the scaling law and the experimental data.

1. Introduction

The systematic study of the dynamics of particles in viscoelastic fluids started over half a century ago [1,2] with earlier works mainly reporting experimental observations, in simple flow cells, of complex behaviours, such as migration and accumulation of the particles. The experimental results were also qualitatively supported by theoretical predictions derived under the conditions of slow and slowly varying flow, and of small particle size [1–4]. The development of more accurate experimental techniques, like particle velocimetry, allowed the detailed analysis of the dynamics of the particles in a wide range of flow conditions. Accurate simulations were also made feasible by the development of numerical algorithms capable of treating non-Newtonian fluids. As a result, several aspects of the particle motion in viscoelastic media have since been understood, especially for simple particle shapes, such as spheres. An accurate work reviewing a large part of the literature on this subject is that by D'Avino and Maffettone [5]. The main conclusion of the aforementioned studies is that migration is observed when there is an imbalance of viscoelastic normal stresses around the particles. This imbalance can be caused by the non-uniformity of the flow field in which the particles are immerged and/or by the particle-wall interactions. If present, the shear-thinning of the ambient fluid influences both the direction and velocity of the migration process . The effect of secondary flows has also been investigated, mainly by considering the migration of a sphere immerged in the pressure-driven channel flow of a viscoelastic fluid [6–8]. According to these studies, the secondary flow drastically changes the migration dynamics by affecting velocity, trajectory and equilibrium position of the particles.

In a recent study, Weheliye et al. [9] used a combination of particle image velocimetry (PIV) and particle tracking velocimetry (PTV) to study the different behaviors of solid particles stirred in Newtonian and viscoelastic ambient fluids. The solid phase consisted of monodisperse PMMA particles with a diameter of 1.5 mm, while the mixing system was an unbaffled cylindrical vessel stirred by a dual-blade paddle impeller. It was found that in a viscoelastic fluid the particles tended to accumulate at the centre of the vortices created by the impeller. The speed of this process was found to be related to the viscoelasticity of the flow; in particular, the dimensionless time scale of the migration process (equal to the time scale of the process multiplied by the impeller rotational speed) decreased exponentially with the Weissenberg number (equal to the relaxation time of the ambient fluid multiplied by the impeller rotational speed). Although Weheliye et al. [9] reported for the first time on the viscoelasticity-induced particle migration in complex three-dimensional flows in stirred vessels, they only presented a qualitative relation between the migration speed and the viscoelasticity of the flow. The difficulty in obtaining accurate values for the migration time was the limiting factor for any quantitative analysis. As reported by the authors, this difficulty arose because the initial dispersion process of the particles in the ambient fluid overlapped with the beginning of the particle migration process. In this paper, we report on experiments that overcome this limitation and allow estimating the particle migration time accurately. Additionally, we present a heuristic argument similar to

* Corresponding author.
E-mail addresses: l.mazzei@ucl.ac.uk (L. Mazzei), p.angeli@ucl.ac.uk (P. Angeli).

https://doi.org/10.1016/j.jnnfm.2022.104918
Received 21 March 2022; Received in revised form 30 July 2022; Accepted 6 September 2022
Available online 9 September 2022

Table 1
Composition and physical properties of the ambient fluids.

	Glycerol (%)	Water (%)	$ZnCl_2$ (%)	ρ (kg/m^3)	η_0 (Pa s)	η_p (Pa s)	λ (ms)
GW	96	4	-	1236	0.51	-	-
GW100	98	2	-	1237	0.58	0.017	21
RI100	16	39	45	1640	0.75	0.010	3.5

that of D'Avino and Maffettone [5] to derive, via scaling, a novel expression for the particle migration velocity in stirred vessels. To verify the applicability of this expression, we employed two sets of planar PIV measurements to reconstruct the three-dimensional flow field created in an unbaffled cylindrical vessel by the rotation of a Rushton turbine, in both Newtonian and viscoelastic fluids. The Rushton turbine was chosen as a midpoint between the simple flows usually encountered in the literature for viscoelasticity-induced particle migration and the complex flow fields generated in industrial mixers. In particular, this turbine generates a well-characterized, three-dimensional flow field that can be easily studied in terms of its main directions of strain. To isolate the effect of normal stresses from other non-Newtonian properties (i.e. shear-thinning), we limited the study to viscoelastic fluids with constant viscosity (Boger fluids). The conditions of the migration tests were chosen to minimize the effect of both gravity and inertial forces on the particle dynamics. The characteristic time of particle migration predicted by the scaling equation was compared with the experimental data obtained in a wide range of fluid elasticity, impeller diameter and impeller speed. The experimental particle migration velocity was accurately measured via particle tracking (PT) experiments that allowed the estimation of the degree of dispersion of the solid phase and its change in time.

2. Experimental setup

2.1. Systems and flow geometry

The experiments were conducted in a flat-bottomed cylindrical vessel with a diameter $T = 50$ mm. The fluid was stirred with two different standard Rushton turbines with a diameter D of 17 and 35 mm. The impeller clearance from the bottom and the liquid height were 25 and 50 mm, respectively. To minimize the optical distortion arising from the curvature of the tank, we enclosed the vessel in a square trough filled with glycerol. The vessel, the trough and the 17 mm impeller were made of transparent acrylic material to maximize the volume of fluid accessible for measurements, while the 35 mm impeller was made of stainless steel. The solid phase consisted of acrylic spherical particles (density of 1.2 g cm^{-3}) with a diameter d_p of 500 μm coated in Rhodamine B (Cospheric). The difference between the refractive index of pure glycerol (1.475) and the acrylic (1.495) was small enough to discount the effect of the light refraction on the images. Both the PIV and PT experiments were conducted using the same optical setup consisting of a continuous diode laser, a mirror and a high-speed camera. The light was generated using a Laserglow5® continuous laser (532 nm, 3000 mW) equipped with a spherical and a cylindrical lens mounted in series to create a 1 mm

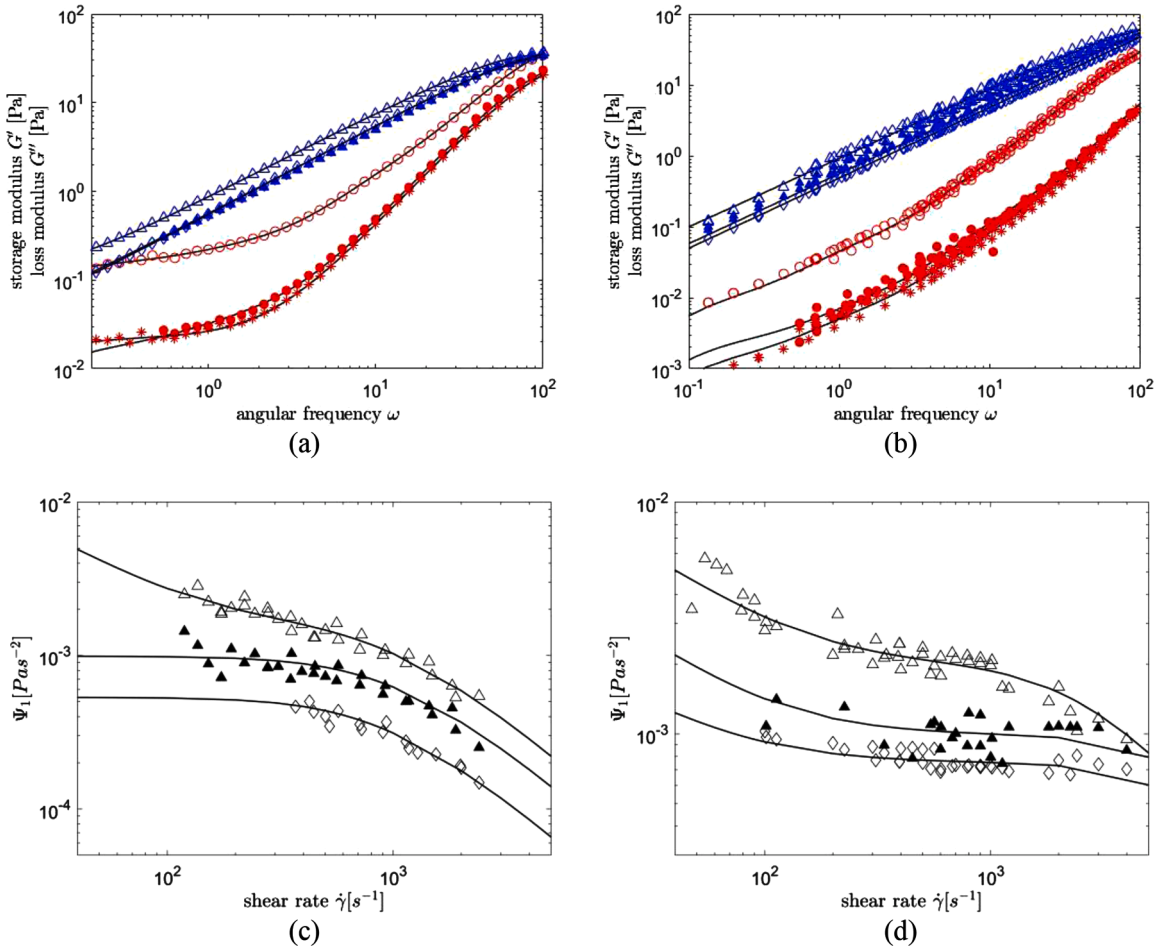

Fig. 1. SAOS experimental data and model fitting at three different stirring times for (a) GW100 and (b) RI100: (Δ) G'' at 0 min; (▲) G'' at 30 min; (◊) G'' at 90 min; (○) G' at 0 min; (●) G' at 30 min; (◊) G' at 90 min. Simple shear experimental data and model fitting at three different stirring times for (c) GW100 and (d) RI100: (Δ) Ψ_1 at 0 min; (▲) Ψ_1 at 30 min; (◊) Ψ_1 at 90 min.

laser sheet. A Phantom high-speed camera was equipped with a 105 mm Nikon lens resulting in a spatial resolution of 50 μm/pixel. Finally, an orange filter was connected to the camera lens to eliminate any reflections of the laser light.

2.2. Rheology

Three ambient fluids were used. A Newtonian reference fluid (GW), made of a mixture of 96% glycerol and 4% water, and two dilute polymer solutions with nearly constant viscosity (Boger fluids). The polymer solutions were obtained by dissolving 100 ppm of polyacrylamide ($M_w = 5–6 \times 10^6$ g/mol) in a mixture of glycerol, water and zinc chloride. Compositions and properties of the ambient fluids are reported in Table 1, while details about the preparation procedure can be found in Weheliye et al. [9]. In Table 1, η_p and η_0 are the polymer contribution to the viscosity and the total viscosity of the mixture, while λ denotes the fluid relaxation time.

To characterize the viscoelastic behavior of the polymer solutions, we conducted two tests: small-amplitude oscillatory shear (SAOS) and steady-state simple shear tests. Both were conducted on an Anton Paar MCR302 rotational rheometer at a temperature ranging from 0 to 70 °C for the shear tests and from 10 to 50 °C for the SOAS tests. The larger temperature range required for the simple shear tests is motivated by the very small values of normal forces exhibited by the dilute polymer suspensions in the range of shear rate normally accessible by the rheometer (0.01–100 s^{-1}). All the data obtained at different temperatures were shifted to the reference temperature of 23 °C through the method of reduced variables [10]. This technique enabled the extension of the interval of shear rates or angular frequencies accessible for the measurements. The rheometer was equipped with a 50 mm parallel plate (PP) for the steady-state simple shear tests and a 50 mm cone and plate (CP) measuring system for the SOAS tests. The PP system allowed the use of the thermal expansion compensation function of the instrument, which automatically adjusts the gap between the plates when the temperature is changed. This function allowed conducting the sequence of shear tests at different temperature on a single fluid sample. The non-uniformity of the shear-rate profile inside the gap of the PP system required the use of the Rabinowitsch-Mooney correction, which was automatically performed by the software of the rheometer.

Polymer solutions are susceptible to mechanical degradation when subject to intense shear for a prolonged time. The degradation is caused by the breaking of the long molecular chains of the suspended polymer and results in a drastic change of the rheological properties of the ambient fluid [11]. To estimate the magnitude of this degradation, each fluid was subjected to intense stirring at 1500 RPM for 1.5 h into our mixing system, while the rheological properties were measured at regular intervals of 30 min. To estimate the relaxation times, we fitted the experimental data with the multimode Giesekus constitutive equation, with a number of modes between 1 and 3. The multimode Giesekus model was preferred to the more common multimode Maxwell model because it was able to successfully predict both the linear viscoelastic properties obtained by the SAOS tests and the non-linear shear-thinning of the first normal stress coefficient obtained in the steady-state simple shear tests.

The results of both the SAOS and the simple shear experiments for the two viscoelastic fluids are reported in Fig. 1. A high degree of polymer degradation can be detected after 30 min of stirring. This is clearly showed by the sizable reduction in storage modulus for both GW100 (Fig. 1 – (a)) and RI100 (Fig. 1 – (b)). The overlapping between the curves obtained after 30 min and 1.5 h indicates that most of the mechanical breaking of the polymer chains happens in the first half hour of stirring. After this time, no further degradation is evident. It is interesting to notice that the value of the loss modulus does not change considerably due to the polymer degradation; this is because the impact of the polymer degradation on the value of the total viscosity of the solution is relatively small. A corresponding reduction of the first normal stress coefficient can also be observed for both fluids (Fig. 1 – (c) and (d)). In a similar way, it appears that most of the reduction of the normal force is observed after 30 min of stirring although some degradation is still observed after 90 min. Finally, the close fit between the data predicted by the model and the experimental results proves that the polymer solution can be successfully modelled with the Giesekus constitutive equation.

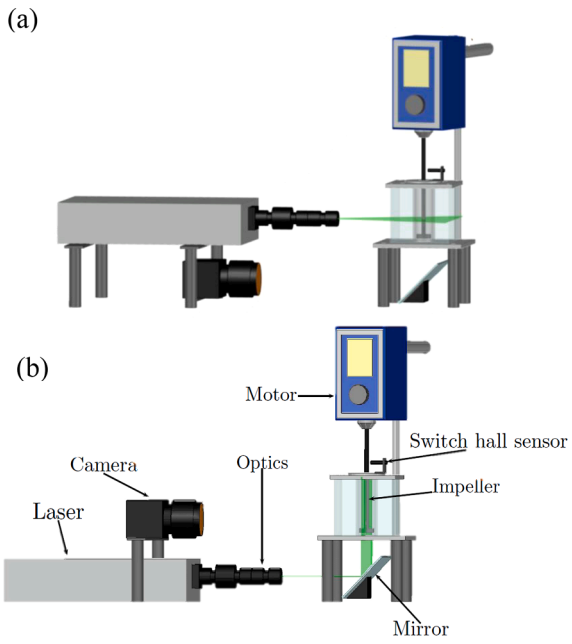

Fig. 2. PIV setups for the horizontal measurements (a) and vertical measurements (b).

As we will show in Section 3.2, the migration of the solid phase can last up to 40 minutes. Considering the previous results, we conclude that the polymer degradation and the relative change of the fluid relaxation time would seriously hinder the estimation of the Weissenberg number (Wi) of the flow. To account for this phenomenon, prior to any migration test, the polymer solution was loaded in the mixing system and stirred for 90 min at 1500 RPM. At the end of this phase, the breaking of the polymer chains was assumed to be complete. Finally, all the rheological properties considered depend strongly on the fluid temperature. To assess the extent of the temperature change induced by the mechanical stirring, the temperature of the fluid was measured at the beginning and at the end of each test. For all the conditions considered, the temperature difference was found to be below 2 °C. The final values of the viscosity and relaxation time were then considered constant throughout the experiments.

2.3. Particle image velocimetry

The reconstruction of the 3D velocity field was carried out for the Newtonian reference fluid and the GW100 viscoelastic fluid. It was assumed that the effect of the fluid viscoelasticity on the fluid dynamics inside the tank only depends on the polymer concentration via the value of Wi and is not affected by the composition of the Newtonian solvent in which the polymer is dissolved. For this reason, the fluid RI100 was not subjected to the PIV tests.

The two mixtures were stirred with the 35 mm Rushton turbine at two impeller speeds, N=333 rpm and 666 rpm; this corresponds to Wi = 1.15 and 2.3 for the fluid GW100 at 333 and 666 rpm, respectively. As tracers for the PIV measurements, we used fluorescent polymer particles with 20 μm diameter made of melamine resin and coated with Rhodamine B, which at room temperature has a high fluorescent intensity. For the experimental conditions investigated, the tracer relaxation time was

negligible compared to the convection time ($St = \frac{\rho_t d_t^2}{18\eta_0} N \ll 1$, where ρ_t and d_t are the tracer density and diameter, respectively). Concurrently, the terminal velocity and the slip velocity resulting from inertial effects are several orders of magnitude smaller that the fluid velocity, guaranteeing that the tracer rapidly relaxes to the local value of the fluid velocity. Schematic diagrams of the PIV setups for the horizontal and vertical plane measurements are provided in Fig. 2 (a) and (b), respectively. In the remainder of the paper, a cylindrical coordinate system (r, θ, and z) with origin in the center of the base of the vessel will be used.

To reconstruct the velocity field, we conducted two sets of 2D PIV tests in the horizontal and vertical directions. Several works in the literature report on the flow field produced by a Rushton turbine in conditions similar to those investigated in this work [12–16]. Some of these works use stereo-PIV to measure the entire 3D velocity field in the vessel. Although this technique has been extensively validated, in the present work it was found that the use of 2D PIV measurements ensured a higher spatial resolution for the measured vector field.

The horizontal PIV measurements were carried out at intervals of $\Delta z/T = 0.02$ in the height interval $z/T = 0$–0.48. At the beginning of each test, the position of the laser plane was adjusted at the desired z level. The image capture was then synchronized with the impeller position using a hall switch sensor. This allowed capturing images at a fixed impeller phase angle θ (i.e. the azimuthal angle or rotation of the impeller around the vertical axis z) equal to 0^o. A total of 100 images pairs (corresponding to 100 impeller rotations) were captured for each horizontal plane; on each plane, the velocity field was then obtained by averaging the 100 instantaneous vector fields.

The vertical velocity field was obtained through time-resolved measurements. In this case, the laser plane was kept in the same vertical position throughout the tests (that is, just one vertical plane was considered) and the image acquisition was not synchronized with the impeller phase angle. A total of 3000 images were captured with an acquisition rate f of 1000 Hz and 2000 Hz for $N = 333$ rpm and 666 rpm, respectively. This allowed obtaining images with a resolution $\Delta\theta = 2^o \left(\frac{N}{60}\frac{360}{f}\right)$ for a total of 90 planes. The displacement of the tracer between the images at θ_i and θ_{i+1}, with $i = 1,\ldots,90$ was used to calculate the velocity field at the angle $\frac{\theta_i + \theta_{i+1}}{2}$. For each phase angle, a total of 33 velocity fields were obtained and subsequently averaged. The independence of the PIV results from the sample size is shown in Fig. A2 in Appendix A.

Each velocity field was calculated from the tracer displacements between two consecutive images with the freeware package JPIV, using a 50% window overlap for a final interrogation window with resolution of 16×16 pixels. An amplitude filter was applied to each cross-correlation box to eliminate the vectors that substantially deviated from the median value. Note that both the u_r and u_z components of the fluid velocity along the θ direction were directly available from the vertical measures, while the horizontal tests provided u_r and u_Θ along the z direction. In order to obtain the full 3D velocity field in the stirred tank, we first azimuthally stacked the vertical measurements. Subsequently, the horizontal measurements were stacked along the z direction. The exact placement of the horizontal velocity vectors was decided by comparing the values of the u_r components obtained from both the horizontal and the vertical measurements.

2.4. Particle tracking

The particle tracking experiments were performed with the optical system in the configuration shown in Fig. 2 - (b). The objective of these tests was to determine the particle migration time as a function of the Weissenberg number defined as the product of the fluid relaxation time and the characteristic value of the shear rate ($Wi \equiv \lambda\dot{\gamma}_c$). The characteristic value of the shear rate was chosen as the average shear rate in the fluid surrounding the impeller. This value was calculated according to Metzner and Otto [17] as follows:

$$\dot{\gamma}_c = k_s N \tag{1}$$

where k_s is the Metzner and Otto constant that depends on the shape of the impeller. Although Eq. 1 was originally derived for inelastic shear-thinning fluids, Seyssiecq et al. [18] derived the values of k_s for a Rushton turbine for a wide array of viscoelastic fluids. Their work reports a value of k_s ranging from 9 to 12. In this work we only intend to capture the order of magnitude of the migration velocity, hence we assumed a value of $k_s = 10$. Finally, the migration time is defined as the time at which no significant change in the distribution of the particles can be detected. Experiments were conducted with both the 17 mm and the 35 mm turbines at a rotation speed N ranging from 200 to 1200 rpm. This resulted in Wi values between 0.05 and 2 and $Re \equiv \frac{\rho_f N D^2}{\eta_0}$ values between 5 and 15. At the beginning of each test, 1.5 g of acrylic spheres (equivalent to a volume fraction of 1%) were placed on the liquid surface. The system was then stirred at 2000 rpm for 5 min until a homogeneous particle distribution was achieved. At this point, the impeller speed was adjusted to the desired value and the recording was started. The PT tests were performed with the impeller phase angle locked at 0°. The images were acquired with a frequency of 0.6 Hz for a time ranging from 15 min to 2 h depending on the impeller velocity and the migration speed. Fig. 3 - (a) shows a typical raw image obtained from a PT experiment for the fluid RI100 at Wi = 1.33. The bright circles correspond to the suspended solid particles. Based on the intensity histogram of the raw image, we used a threshold value to binarise the images and isolate the solid spheres. To detect the edges of the solid particles, a circular Hough transform algorithm (CHT) was employed. The CTH algorithm provided the position and the diameter of all the solid particles crossing the 1 mm laser plane. In order to account only for the particles that fully cross the laser plane, all the spheres with a diameter lower that 0.5 mm were discarded. The image shown in Fig. 3 - (b), clearly displaying the position of the particles, was then used for the analysis of the migration phenomenon. The degree of dispersion of the solid phase was estimated through the use of the Shannon entropy function (S^*):

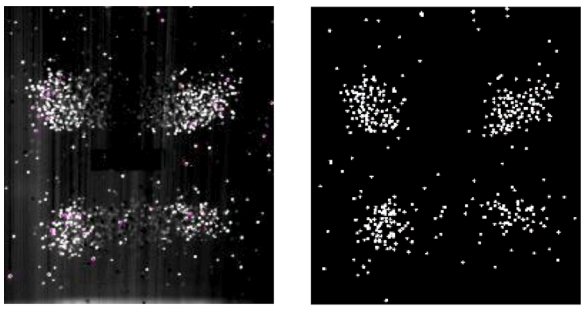

Fig. 3. (a) raw PT image; (b) image with the detected solids for RI100 at Wi = 1.33.

$$S^* = \sum_{i=1}^{M}\sum_{j=1}^{2} p_j(i) ln\left(p_j(i)\right) \tag{2}$$

where M is the number of sub-regions in which the image is divided, and $p_j(i)$ is the ratio between the number of pixels occupied by the j-th phase and the total number of pixels in the ith sub-region. A more detailed description of this function and its calculation are reported in [9].

2.5. Strain rate tensor

The scaling law that we will propose in Section 3.3 is derived for a spherical particle immerged in a bi-dimensional, rotating shear flow. However, usually the flow field created by a rotating turbine is complex

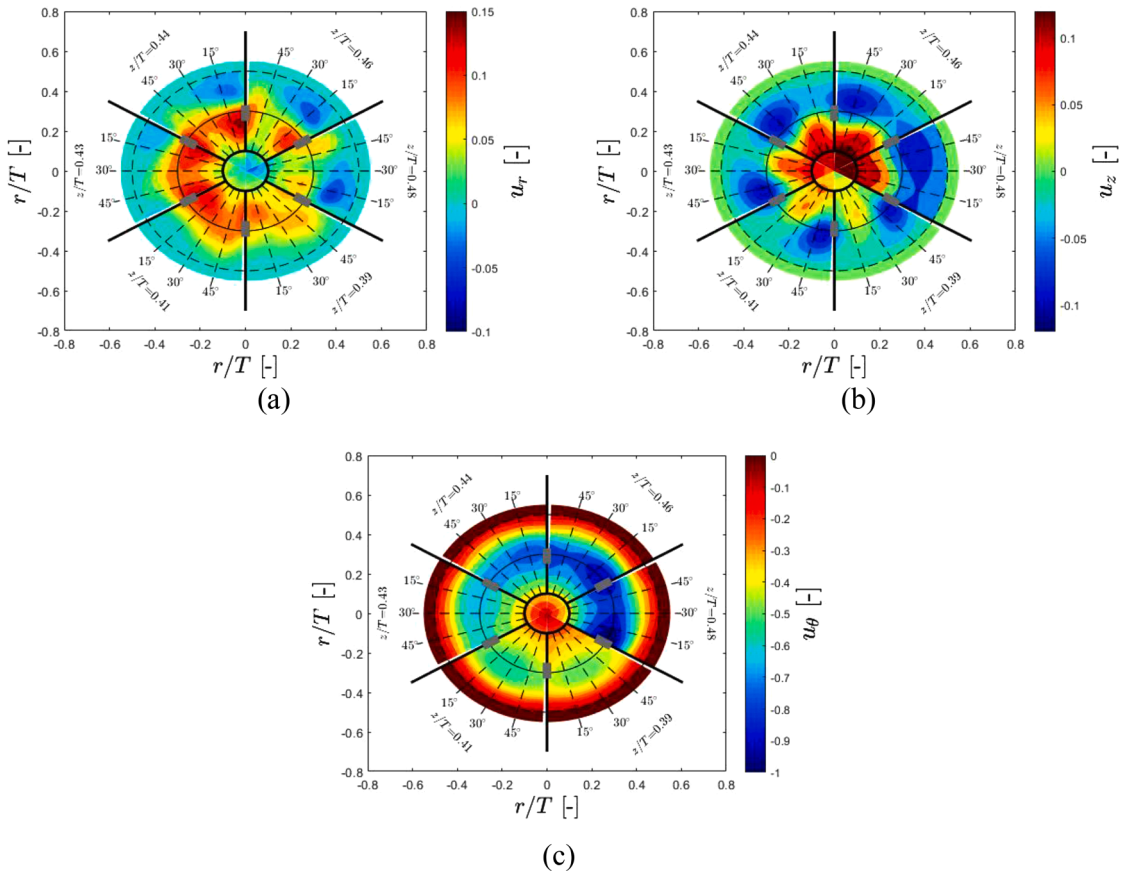

Fig. 4. Dimensionless radial (a), axial (b) and angular (c) components of the velocity field for the fluid GW100 at Re = 4.3 and Wi = 0.44.

and three-dimensional. In order to assess the extent to which the flow field created by a Rushton turbine can be conceptually reduced to a bi-dimensional rotating shear flow on the *r*-θ plane, we analysed the rate of strain (or deformation) tensor field. The velocity gradient ($\nabla \boldsymbol{u}$) can be decomposed into a symmetric part $\dot{\boldsymbol{\gamma}}$, usually called strain rate tensor, and an antisymmetric part $\boldsymbol{\Omega}$, referred to as rotation rate tensor. The physical components of the strain and rotation rate tensors with respect to a cylindrical coordinate system are reported in the following equations:

$$\dot{\gamma} = \begin{pmatrix} \frac{\partial u_r}{\partial r} & \frac{1}{2}\left[r\frac{\partial}{\partial r}\left(\frac{u_\theta}{r}\right)+\frac{1}{r}\frac{\partial u_r}{\partial \theta}\right] & \frac{1}{2}\left[\frac{\partial u_r}{\partial z}+\frac{\partial u_z}{\partial r}\right] \\ \frac{1}{2}\left[r\frac{\partial}{\partial r}\left(\frac{u_\theta}{r}\right)+\frac{1}{r}\frac{\partial u_r}{\partial \theta}\right] & \frac{1}{r}\frac{\partial u_\theta}{\partial \theta}+\frac{u_r}{r} & \frac{1}{2}\left[\frac{1}{r}\frac{\partial u_z}{\partial \theta}+\frac{\partial u_\theta}{\partial z}\right] \\ \frac{1}{2}\left[\frac{\partial u_r}{\partial z}+\frac{\partial u_z}{\partial r}\right] & \frac{1}{2}\left[\frac{1}{r}\frac{\partial u_z}{\partial \theta}+\frac{\partial u_\theta}{\partial z}\right] & \frac{\partial u_z}{\partial z} \end{pmatrix} \tag{3}$$

$$\Omega = \frac{1}{2}\begin{pmatrix} 0 & \omega_z & -\omega_\theta \\ -\omega_z & 0 & \omega_r \\ \omega_\theta & -\omega_r & 0 \end{pmatrix} \tag{4}$$

where the vorticity $\boldsymbol{\omega}$ is defined as:

$$\omega = \left(\frac{1}{r}\frac{\partial u_z}{\partial \theta}-\frac{\partial u_\theta}{\partial z}\right)i_r + \left(\frac{\partial u_r}{\partial z}-\frac{\partial u_z}{\partial r}\right)i_\theta + \left(\frac{1}{r}\frac{\partial}{\partial r}(ru_\theta)-\frac{1}{r}\frac{\partial u_r}{\partial \theta}\right)i_z \tag{5}$$

where $\boldsymbol{i_r}$, $\boldsymbol{i_\theta}$ and $\boldsymbol{i_z}$ are (mutually normal) unit vectors in the r, θ and z directions, respectively. Following the approach proposed by Bouremel et al. [19], we calculated the principal components of the strain rate tensor (Eq. 6) to analyse the strain dynamics in different regions of the vessel.

$$\nabla u = \begin{pmatrix} S_{11}^* & 0 & 0 \\ 0 & S_{22}^* & 0 \\ 0 & 0 & S_{33}^* \end{pmatrix} + \frac{1}{2}\begin{pmatrix} 0 & \omega_3^* & -\omega_2^* \\ -\omega_3^* & 0 & \omega_1^* \\ \omega_2^* & -\omega_1^* & 0 \end{pmatrix} \tag{6}$$

with S_{11}^*, S_{22}^* and S_{33}^* the eigenvalues of $\dot{\boldsymbol{\gamma}}$ and ω_1^*, ω_2^* and ω_3^* the components of the vorticity vector along the local principal axes of the strain rate tensor. The local principal axes are defined by the eigenvectors associated with the eigenvalues S_{11}^*, S_{22}^* and S_{33}^*. The change of vector basis allows identifying the local velocity of deformation in the directions of the principal axes (i.e. velocities of stretching or compression). In particular, if $S_{ii}^* > 0$ (no summation over the index i is implied) the fluid element is stretched in the i direction, whereas if $S_{ii}^* < 0$, it is compressed. The values of the three components of the strain rate tensor can also be used to assess the intensity of the deformation in the three principal directions relative to each other. In particular, if one of the three components is small compared to the other two, the deformation field can be essentially regarded as bi-dimensional.

3. Results

3.1. Velocity field and flow structure

An overview of the three components of the velocity field for the fluid GW100 at Re = 4.3 and Wi = 0.44 is reported in Fig. 4. All the velocities are normalised with the impeller tip speed πDN. The fluid is stirred with the 37 mm Rushton turbine. The 37 mm impeller was made of stainless steel; therefore, only the lower part of the tank was accessible to measurements. To provide sufficient information about the flow field, we divided both plots in six sectors, each reporting the component

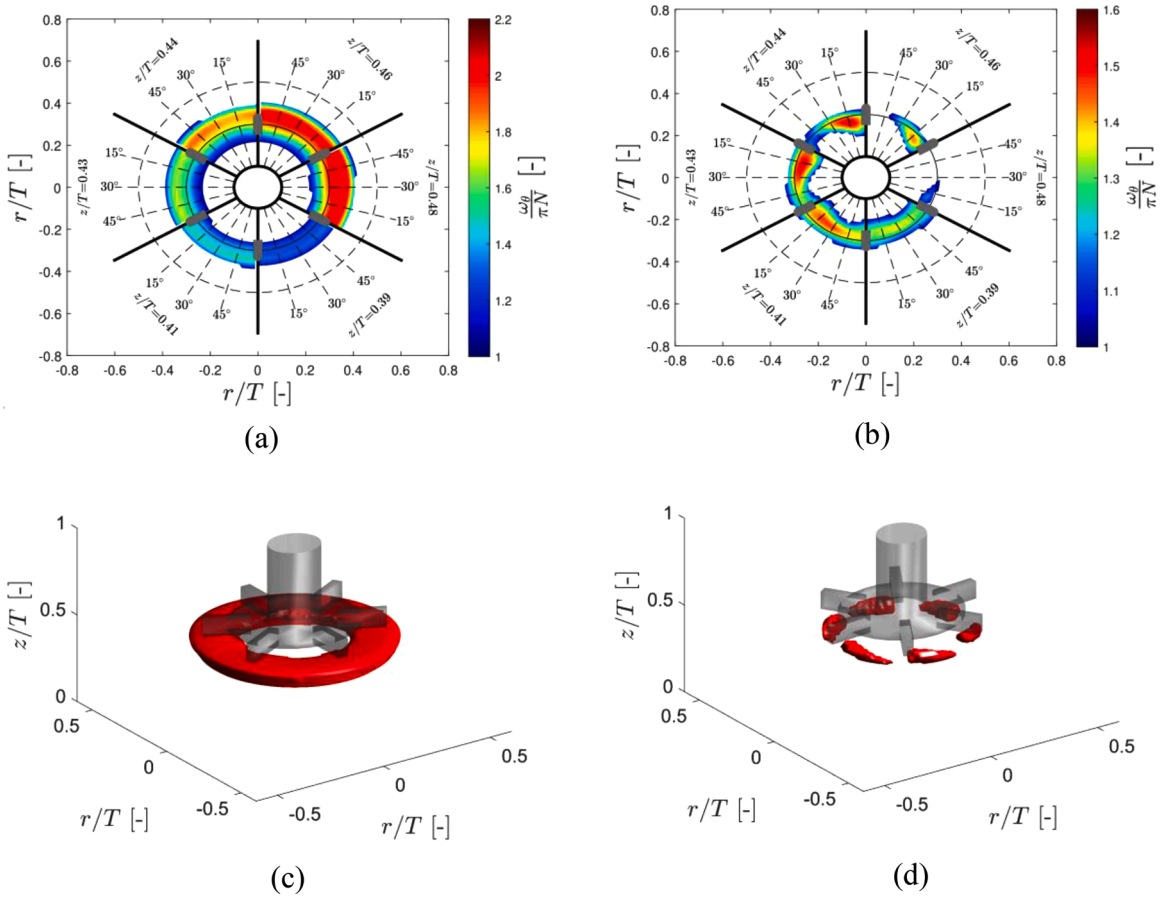

Fig. 5. Vorticity plot and vortex structure for GW (a) and (c) and GW100 (b) and (d) at Re = 4.3 and Wi = 0.44. In both cases, the impeller rotates in the clockwise direction.

of the velocity over an angle of 60° for six axial positions z/T (i.e. 0.39, 0.41, 0.43, 0.44, 0.46 and 0.48) with the axial coordinate decreasing counter-clockwise and impeller rotating in the clockwise direction. The overall flow can be described as the superposition of a rotational flow around the z axis and of a rotational flow in the r-z plane. In this plane, the fluid moves in the positive r direction with the maximum radial velocity in correspondence of the edge of the palettes of the impeller. The fluid then slows down as it approaches the walls of the vessel. On reaching the wall, the radial component of the fluid velocity rapidly reduces to zero, while the axial component increases. The stream then divides into two equal parts directed above and below the axial position of the impeller and circulates back returning to the impeller region. Unsurprisingly, the value of the angular component of the velocity is an order of magnitude larger than the other two; hence, the dominating motion is represented by the rotation around the z axis. It is known that unbaffled stirred tanks usually present a central vortex at the liquid-air interface. Given the small value of the Reynolds number, at all the conditions examined the central vortex remains small and confined to a small area around the shaft of the stirrer.

As it will be shown in Section 3.3, the migration of the particles is caused by the presence of an elastic force acting in the radial direction. The intensity of this force is not uniform along the z axis and it reaches its maximum value in the vicinity of the impeller. This means that the secondary flow described above contributes to the dynamics of the migration insofar as it continuously circulates the solids in the r-z plane and leads the particles to move on helicoidal pathlines around the z axis. Fig. 5 – (a) and (b) shows the contour plot of the normalised angular component of the vorticity for both the Newtonian fluid and the viscoelastic fluid GW100 at Re = 4.3 and Wi = 0 and 0.44, respectively. From Fig. 5 - (a) it can be seen that in the Newtonian case the rotation of the turbine creates the characteristic toroidal vortex flow-structure, with the maximum value of the angular vorticity located at the tip of the impeller and at $z/T = 0.48$ and $r/T = 0.35$. The vorticity then decreases when moving further away from the impeller both in the radial and in the axial directions. Note that the vortex created by the turbine interests the volume of fluid from $r/T = 0.2$ to $r/T = 0.40$ and only gradually decreases in intensity when moving further away along the z direction.

As Fig. 5 – (b) shows, the viscoelasticity of the fluid substantially changes the shape of the vortical structures. In particular, the toroidal vortex present in the Newtonian case loses its continuity and breaks into smaller trailing vortices that depart from the tip of the turbine. The intensity of the vorticity is also reduced, the maximum value of the normalised angular component reducing from 2.2 for the Newtonian case to 1.6 for the viscoelastic case. It can also be observed that the centre of the vortex shifts in both the radial and axial directions and is now located at $z/T = 0.44$ and $r/T = 0.3$. The difference between the two flow fields can be clearly observed in Fig. 5 – (c) and (d), where the three-dimensional structure of the vortex is shown by plotting iso-vorticity surfaces at $\omega_\theta/\pi N = 1.5$.

The contour plots of the principal components of the strain rate tensor S^*_{11}, S^*_{22} and S^*_{33}, for the fluid GW100 at Wi = 0.44 are shown in Fig. 6 (a)-(c) for six values of z/T. The strain rate S^*_{11} is positive over the entire plane of measure, while S^*_{22} is everywhere negative. This indicates that the fluid is always stretched along the principal direction associated with S^*_{11} and compressed along the direction associated with S^*_{22}. On the other hand, S^*_{33} changes sign from positive to negative, indicating the presence of both areas of stretching and compression. The strain rates S^*_{11} and S^*_{22} are always dominant, as their dimensionless absolute values reach a peak of 1.5, while for S^*_{33} it is $-0.4 < S^*_{33}/\pi N < 0.4$. All three strain rates assume local absolute maxima close to the impeller blades for every z/T considered. Although not reported in Fig. 6, it is important to notice that the eigenvectors associated to S^*_{11} and S^*_{22} are

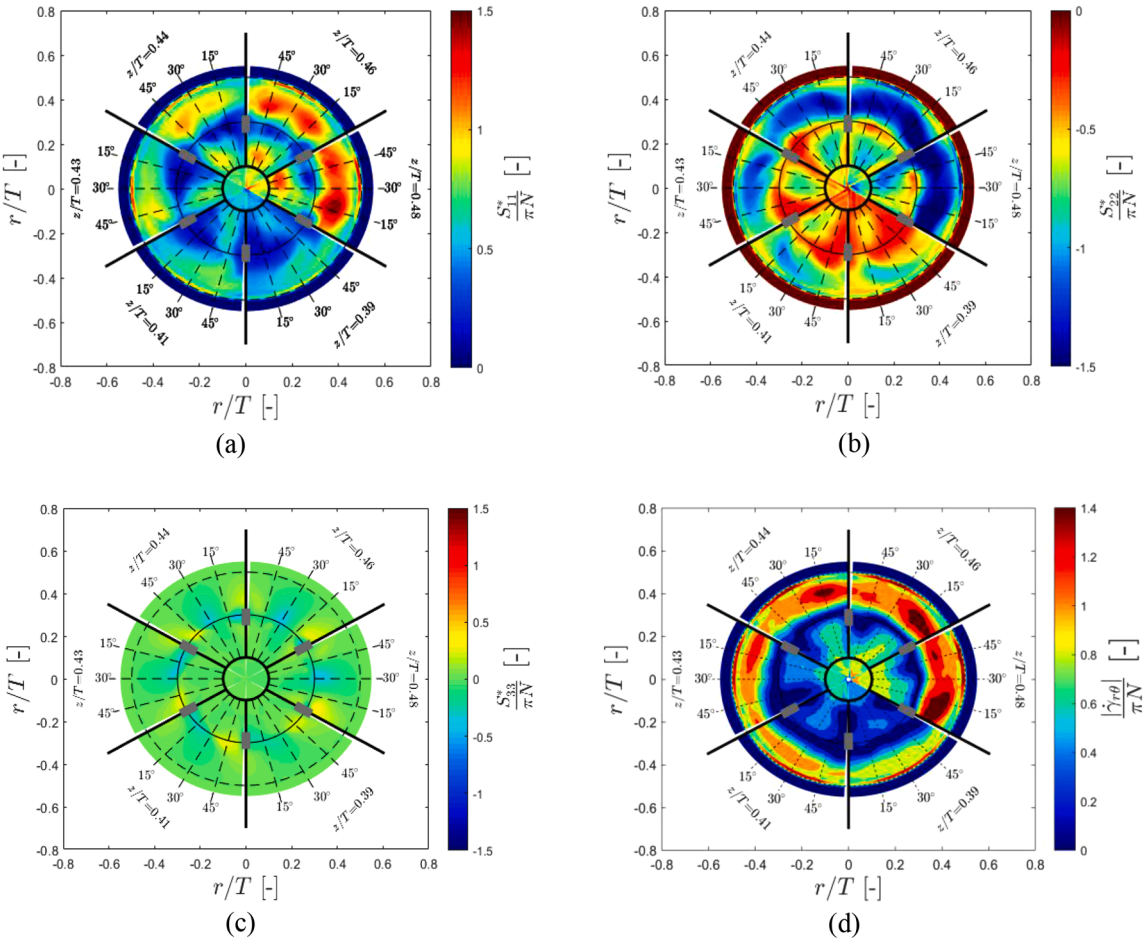

Fig. 6. Normalised principal stresses (a,b,c) and absolute value of the r-θ component of the strain rate tensor (d) for GW100 at Re = 4.3 and Wi = 0.44. The impeller rotates in the clockwise direction.

everywhere parallel to the *r*-θ plane and orthogonal to each other, while the one associated with S^*_{33} is everywhere parallel to the *z* direction. Apart from a small area around the tip of the impeller blades, the strain rate S^*_{33} is everywhere close to zero. This indicates that the local deformation of the flow is essentially bi-dimensional and controlled by two strain rates of stretch and compression mutually orthogonal to each other and parallel to the *r*-θ plane.

As reported by D'Avino and Maffettone [5], one of the necessary conditions for viscoelastic particle migration is the presence of shear rate gradients. In the nearly bi-dimensional rotating shear flow described so far, the only relevant component of the rate-of-strain tensor is that associated with the coordinates *r* and θ. Fig. 6 - (d) reports the normalised, absolute value of this component. It is possible to observe that for every value of *z/T*, the absolute value of $\dot{\gamma}_{r\theta}$ shows a non-monotonic behaviour when moving in the positive *r* direction, with the presence of two areas of maximum and minimum shear. For example, at $z/T = 0.48$, $\dot{\gamma}_{r\theta}$ initially decreases from the value of 1 at $r/T = 0$ to the value of 0 at $r/T = 0.3$, it then increases until reaching its maximum value of 1.5 at $r/T = 0.41$, and then sharply decreases until reaching a value of 0 in correspondence of the wall. Moving along the axial direction, the maximum absolute value of $\dot{\gamma}_{r\theta}$ decreases from 1.5 at

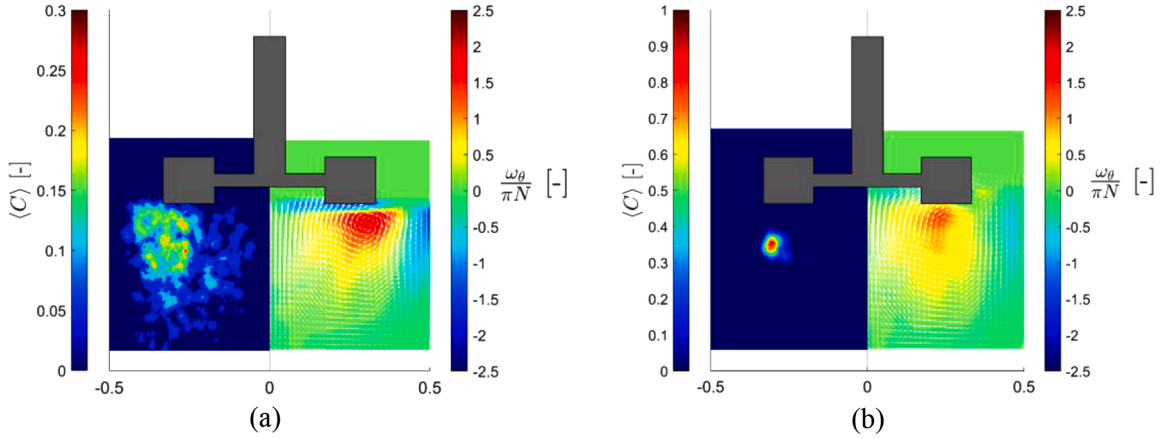

Fig. 7. Vorticity contour plot and particles concentration for GW (a) and RI100 (b) at Re = 10 and Wi = 0 and 0.35, respectively.

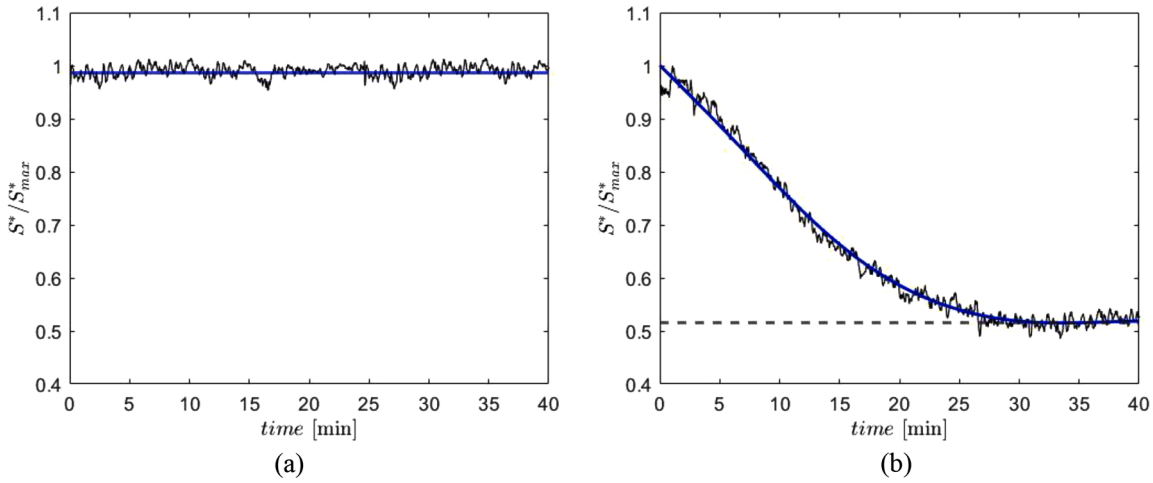

Fig. 8. Normalised Shannon entropy for GW (a) and RI100 (b) at Re = 10 and Wi = 0 and 0.35, respectively.

$z/T = 0.48$ to 1 at $z/T = 0.39$. In addition, the radial position of the maximum of $\dot{\gamma}_{r\theta}$ moves to increasing value of r/T while the size of the area of low shear rates widens. The variation of $\dot{\gamma}_{r\theta}$ is responsible for the migration of the particles in the r-θ plane toward lower absolute value of shear rates.

3.2. Migration experiments

A second set of experiments was carried out to track the distribution of the solid particles in the tank and its evolution in time. At the beginning of each test, the solid particles were placed on top of the liquid surface. The liquid was then stirred at an impeller speed of 2000 rpm for 5 min. After 3 min of stirring at 2000 rpm, the particles were uniformly dispersed throughout the flow. If stirring continues, the Newtonian and viscoelastic systems show two radically different behaviours. Fig. 7 – (a) compares the average solid volume fraction ($\langle C \rangle$) and the normalised angular vorticity contour plots, after 90 min of stirring, for the fluids GW and RI100 at Re = 10 and Wi = 0 and 0.35, respectively. For the Newtonian case, no significant change in the particle distribution is observed. The solids remain uniformly distributed up to 90 min after the stirring is initiated. For the viscoelastic case, on the other hand, Fig. 7 – (b) shows an accumulation of the solid phase at the centre of the vortex created by the rotation of the impeller.

The migration velocity was estimated by calculating the degree of disorder of the liquid-solid system represented by the Shannon entropy index (S^*). Fig. 8 (a) and 8 (b) shows the evolution of the Shannon entropy with time for the Newtonian fluid, GW, and for the viscoelastic fluid, RI100, at Re = 10 and Wi = 0 and 0.35, respectively. In these graphs, the time $t = 0$ corresponds to the moment at which the impeller rotational velocity is reduced from 2000 rpm to the desired final value. At the conditions of the experiments, the particles Stokes number ($\mathrm{St} \equiv \frac{\rho_s d_p^2}{18\eta_0} N$) was much less than unity; thus, the velocities of the particles relax rapidly to their dynamic equilibrium values. If the particles have the same density as the ambient fluid (which is the case for the fluid GW100), this equilibrium value is equal to the local velocity of the fluid. Although the density of the fluid RI100 is higher than the density of the solids, both the particle terminal velocity of the spheres $\left(v_t = \frac{g d_p(\rho_s - \rho_f)}{18\eta}\right)$ and the slip velocity induced by inertia are still negligible compared to the fluid velocity $\left(\frac{v_t}{\pi N} \approx 10^{-5};\ \frac{v_i}{\pi N} \approx 10^{-3}\right)$. We can then assume that in both fluids (GW100 and RI100) the particles rapidly relax to the local equilibrium and that when this happens, the effect of gravity and inertia are negligible. At this stage, the particles are uniformly dispersed into the flow and no migration is evident. To facilitate the comparison, the value of S^* was normalised by dividing it by the maximum value reached during the mixing. In both cases, S^* assumes its maximum value at the beginning of the experiment. For the Newtonian case, there is no appreciable change of S^* throughout the duration of the test (that is, the particles are uniformly dispersed in the liquid and remain that way); S^*/S_{max} remains almost constant at a value of 1 with fluctuation of ± 3%. Contrarily, the Shannon entropy for the viscoelastic fluid reduces sharply from the initial value of 1 at $t = 0$ to the value of 0.54 at $t = 30$ min. This decrease reflects the reduction of the region of the tank occupied by the particles and can be used to estimate the time required for the particle cross-streamline migration. In particular, the final

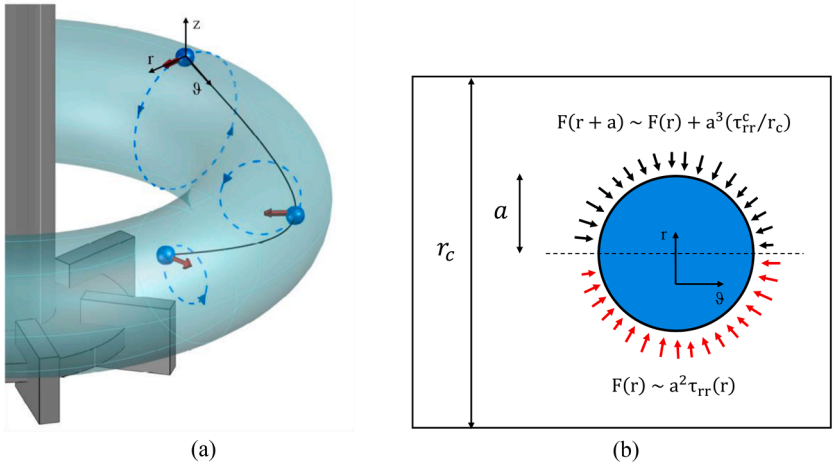

Fig. 9. (a) Particle path line in the stirred vessel and (b) schematic of the elastic force on the sphere.

migration time is taken to be the time at which the Shannon entropy reaches 99% of its final value.

3.3. Scaling law for viscoelasticity-induced particle migration

Here, we propose a simple heuristic argument to understand the nature of particle migration in stirred vessels and identify the parameters that influence this phenomenon.

Consider a nonuniform two-dimensional shear flow, for example that created in the gap between two concentric cylinders (Taylor-Couette flow), where the inner cylinder rotates with an angular velocity Ω while the outer cylinder is stationary. Consider a sphere of radius a and density ρ_s moving in the streamwise (θ) direction at the same velocity as the fluid (Fig. 9 – (b)). We assume that the particle is neutrally buoyant, so that its density is the same as the fluid density (ρ_f). In the absence of forces acting on the sphere in the direction normal to the flow (r direction), the particle would simply move along with the fluid in a circular trajectory concentric with the two cylinders. Experimental evidence ([3,20–25]) shows that if the suspending fluid is viscoelastic, the particle moves towards the decreasing shear rate direction, i.e. towards the outer cylinder. The migration is caused by an imbalance of the viscoelastic normal force acting across the particle. To derive an expression for the migration velocity v_m, we first write a balance of forces on the particle. Divide the sphere in half using an imaginary cutting plane normal to the velocity gradient direction. Each hemisphere is subject to a radial force arising from the fluid elasticity. The magnitude of this force depends on the average shear rate acting on each hemisphere. For the first hemisphere:

$$F(r) \sim a^2 \tau_{rr}(r) \tag{7}$$

where τ_{rr} is the rr-component of stress tensor of the fluid. For the second hemisphere, we write:

$$F(r+a) \sim a^2 \tau_{rr}(r+a) \sim a^2 [\tau_{rr}(r) + a D_r \tau_{rr}(r)] \sim F(r) + a^3 \left(\tau_{rr}^c / r_c\right) \tag{8}$$

Here, τ_{rr}^c is the scale of τ_{rr} and r_c is the characteristic length along which the shear-rate (and thus τ_{rr}) changes significantly. It is assumed that $a/r_c \ll 1$. Then, the total force acting on the particle is:

$$F_E \sim \varepsilon\, a^2 \tau_{rr}^c \tag{9}$$

with $\varepsilon \equiv a/r_c$. This force causes the particle to accelerate in the r-direction and is balanced by the fluid drag force. Assuming that the Stokes law is valid, we can write:

$$F_D \sim \eta_0 a\, v_c \tag{10}$$

where F_D is the drag force, η_0 the fluid viscosity and v_c the velocity scale in the radial direction. At equilibrium, the value of v_c can be obtained by equating Eq. 10 and Eq. 9; this yields:

$$v_c \sim \frac{a \varepsilon \tau_{rr}^c}{\eta_0} \tag{11}$$

All the relations above are expressed in terms of the normal stress scale. This makes sense, insofar as the normal stress is the cause of particle migration. However, it might be useful to eliminate τ_{rr}^c, relating it to the shear rate scale and the fluid viscoelastic properties. If we write the fluid stress tensor as a superposition of solvent and polymer contributions, which is the form usually adopted for polymer solutions ([10, 26]), we have:

$$\tau = \tau_s + \tau_p = -\eta_s \dot{\gamma} + \tau_p \tag{12}$$

Here, $\boldsymbol{\tau}$ is the fluid stress tensor, while $\boldsymbol{\tau}_s$ and $\boldsymbol{\tau}_p$ are the solvent and polymer contributions, respectively. It can be proven that in a bi-dimensional Taylor-Couette flow the rr-component of the stress arises only if $\boldsymbol{\tau}_p$ is different from zero, its exact expression depending on the constitutive model chosen [10]. In general, we can write [10]:

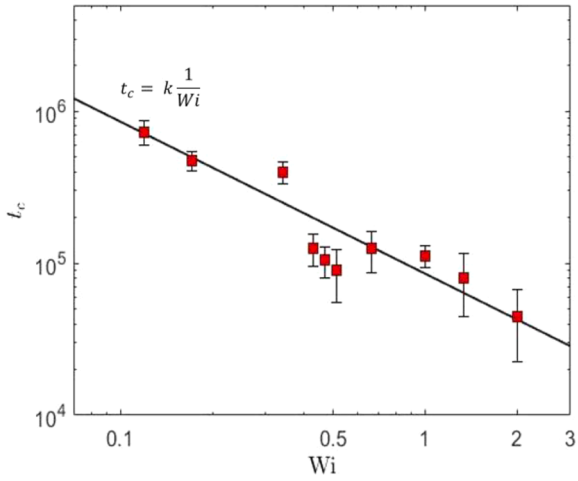

Fig. 10. Dimensionless characteristic migration time as function of the Wi number. Experimental data (red squares) and model prediction.

$$\tau_{rr}^c \sim \eta_p\, \lambda\, \dot{\gamma}_c^2 \tag{13}$$

where η_p is the polymer contribution to the viscosity of the solution, $\eta_0 = \eta_s + \eta_p$, λ is the relaxation time, and $\dot{\gamma}_c$ is the scale of the shear rate. Eq. 13 implies a constant value of the first normal stress coefficient. As shown in Fig. 1 c – d, the liquids used in this study exhibit a shear-thinning of the first normal stress coefficient at high shear rates. Despite this fact, Eq. 13 can still be used in the region of Wi numbers where the first normal stress coefficient remains constant; i.e. Wi < 5 for RI100 and Wi < 7 for GW100. Substituting Eq. 13 in Eq. 11, we obtain:

$$v_c \sim \frac{\eta_p}{\eta_0}\, a\, \lambda\, \varepsilon\, \dot{\gamma}_c^2 \tag{14}$$

Finally, we can rearrange Eq. 14 to derive a direct expression for the dimensionless characteristic migration time $t_c \equiv \frac{r_c}{v_c}\dot{\gamma}_c$:

$$t_c \sim \frac{\eta_0}{\eta_p} \frac{1}{\varepsilon^2 Wi} \tag{15}$$

The scaling law described so far has been derived in the hypothesis of a sphere immerged in a viscoelastic fluid subject to a nonuniform, two-dimensional rotating shear flow. In the previous section, we showed that the three-dimensional flow created by a Rushton turbine in laminar regime can be visualised as the superposition of a main rotational flow around the z axis and a secondary rotational flow in the r-z plane. We also showed that the rate of deformation in the z direction is negligible in comparison to the planar deformation rates in the r-θ plane. This means that, at least with regard to the rate-of-strain tensor, the flow field can essentially be considered bi-dimensional. Furthermore, the variation of $\dot{\gamma}_{r\theta}$ along the radial direction (Fig. 6 - (d)) indicated that in the r-θ plane, the rotating flow is nonuniform.

Fig. 9 (a) shows a schematic representation of the trajectory of the spheres. Following the movement of the liquid, the spheres rotate around both the z axis and in the r-z plane. During their motion, they are subjected to the elastic force arising from the presence of gradients of shear rate in the r-θ plane. These gradients are always oriented along r and directed toward decreasing absolute values of the shear rate. The result is that the spheres move along a spiral pathline ending at the centre of the toroidal vortex created by the impeller.

To apply Eq. 15 to the stirred vessel, we need to assign a value to all the characteristic quantities involved. The characteristic shear rate $\dot{\gamma}_c$ was chosen as the average shear rate defined in Eq. 1 with value of $k_s = 10$, while the characteristic length scale of the flow was assumed equal to the impeller diameter D.

The migration time predicted by the heuristic scaling was validated

against the data obtained from the migration experiments. The results are shown in Fig. 10 in terms of dimensionless characteristic migration time as a function of the Wi number. In agreement with the scaling law, the experimental data show an inverse dependence between t_c and Wi as highlighted by the plotted line $t_c = k/\mathrm{Wi}$. Here, the constant k is used as a simple fitting parameter as the scaling law proposed is only expected to capture the order of magnitude of the time scale of the migration. However, it is interesting to notice that the value of k in Fig. 10 is found equal to 8.55×10^4, very close to the value of $\frac{\eta_0}{\eta_p}\frac{1}{\varepsilon^2}$ that, in the conditions examined, is equal to 8.89×10^4 and 3.67×10^4 for RI100 and GW100, respectively.

4. Conclusions

In this paper, we presented a heuristic argument capable of predicting the characteristic migration time of solid particles suspended in a viscoelastic medium in a stirred vessel. We used planar PIV to reconstruct the three dimensional velocity profile produced by a Rushton turbine in an unbaffled vessel and assessed the effect of the fluid elasticity on the flow field. The reconstruction of the flow field was also used to assess the applicability of the scaling law to the flow in exam. It was found that the velocity field could be reduced to a nonuniform rotating shear flow around the z axis. Particle tracking experiments were also conducted in order to estimate the degree of dispersion of the solid phase and its evolution in time. In accordance with the literature, the experimental data confirmed that in a viscoelastic fluid the solid particles migrate across the streamlines and accumulate in areas of low shear rate. The characteristic velocity of this migration was estimated by calculating the degree of dispersion of the solid phase, through the Shannon entropy index, as a function of time. The experimental data were then used to validate the proposed scaling law. The scaling law was tested against data obtained with different viscoelastic fluids, impeller speeds and impeller diameters. The good agreement between the experimental data and the proposed equation confirms the validity of the scaling argument. The results reported in this work show that solid particles immerged in the flow field produced by a Rushton turbine segregate in particular areas of the flow under the effect of the viscoelasticity-induced cross-flow migration. At first glance, this behaviour seems to be an obstacle to the mixing process for which stirred vessels are usually employed. On the other hand, the same phenomenon could be used for the continuous separation of solids from solid-liquid suspensions in those circumstances when settlers and filters prove to be inconvenient. This is especially for the separation of neutrally (or nearly neutrally) buoyant solids immerged in viscous, non-Newtonian fluids (Fig. A1.

Declaration of Competing Interest

The authors declare that they have no known competing financial interests or personal relationships that could have appeared to influence the work reported in this paper.

Data Availability

Data will be made available on request.

Acknowledgment

The authors would like to acknowledge GlaxoSmithKline Consumer Healthcare and the EPSRC formulation grant CORAL (EP/N024915/1) for the financial support given to this project.

Appendix A

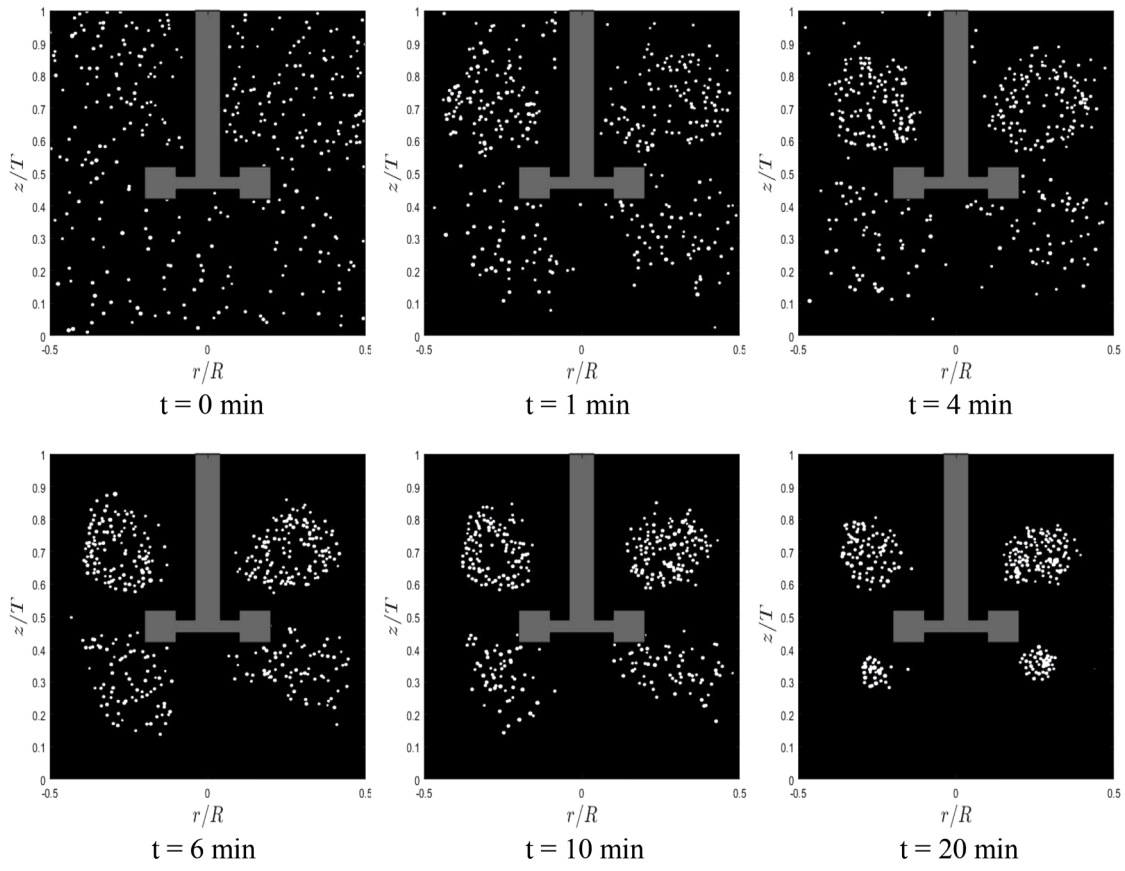

Fig. A1. Time evolution of the particles positions on the horizontal plane for the fluid RI100 at Wi = 0.35.

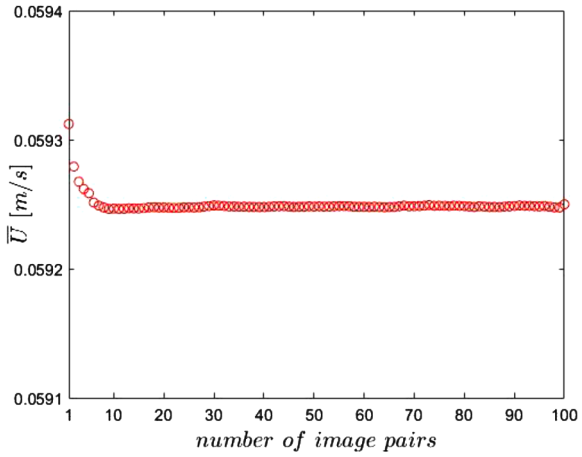

Fig. A2. : Convergence plot for the average velocity on the horizontal plane Z/T = 0.48 for the fluid RI100 at Re = 4.3 and Wi = 0.4, as function of the sample size. The plane at Z/T = 0.48 was chosen as worst case scenario as the convergence of the average planar velocity appears to be faster for all the others horizontal and vertical planes.

References

[1] L.G. Leal, The motion of small particles in non-Newtonian fluids, The Journal of Non-Newtonian Fluid Mechanics 5 (1979) 33–78. C.

[2] P. Brunn, The motion of rigid particles in viscoelastic fluids, The Journal of Non-Newtonian Fluid Mechanics 7 (4) (1980) 271–288.

[3] B.P. Ho, L.G. Leal, Migration of rigid spheres in a two-dimensional unidirectional shear flow of a second-order fluid, The Journal of Fluid Mechanics 76 (4) (1976) 783–799.

[4] P. Brunn, The behavior of a sphere in non-homogeneous flows of a viscoelastic fluid, Rheologica Acta 15 (1976) 589–611, 11–12.

[5] G. D'Avino, P.L. Maffettone, Particle dynamics in viscoelastic liquids, The Journal of Non-Newtonian Fluid Mechanics 215 (2015) 80–104.

[6] G. Li, G.H. McKinley, A.M. Ardekani, Dynamics of particle migration in channel flow of viscoelastic fluids, The Journal of Fluid Mechanics 785 (2015) 486–505.

[7] M.M. Villone, G. D'Avino, M.A. Hulsen, F. Greco, P.L. Maffettone, Particle motion in square channel flow of a viscoelastic liquid: migration vs. secondary flows, The Journal of Non-Newtonian Fluid Mechanics 195 (2013) 1–8.

[8] J. Zhou, I. Papautsky, Viscoelastic microfluidics: progress and challanges, Microsystems & Nanoengineering 6 (1) (2020).

[9] W.H. Weheliye, G. Meridiano, L. Mazzei, P. Angeli, Experimental investigation of the solid-liquid separation in a stirred tank owing to viscoelasticity, Physical Review Fluids 5 (6) (Jun. 2020) 63302.

[10] R. B. Bird, R. C. Armstrong, and O. Hassager, "Dynamics of polymeric liquids. Vol. 1, 2nd Ed.: Fluid Mechanics," vol. 1, no. 18088690, 1987.

[11] K. Mackenzie, A.E. Jemmett, Polymer shear stability, Wear 17 (5–6) (1971) 389–398.

[12] P. Mavros, C. Xuereb, J. Bertrand, Determination of 3-D flow fields in agitated vessels by laser-Doppler velocimetry: use and interpretation of RMS velocities, Chemical Engineering Research and Design 76 (2) (1998) 223–233.

[13] A. Liné, J.C. Gabelle, J. Morchain, D. Anne-Archard, F. Augier, On POD analysis of PIV measurements applied to mixing in a stirred vessel with a shear thinning fluid, Chemical Engineering Research and Design 91 (11) (2013) 2073–2083.

[14] M. Rice, J. Hall, G. Papadakis, M. Yianneskis, Investigation of laminar flow in a stirred vessel at low Reynolds numbers, Chemical Engineering Science 61 (9) (2006) 2762–2770.

[15] H.S. Yoon, D.F. Hill, S. Balachandar, R.J. Adrian, M.Y. Ha, Reynolds number scaling of flow in a Rushton turbine stirred tank. Part I - mean flow, circular jet and tip vortex scaling, Chemical Engineering Science 60 (12) (2005) 3169–3183.

[16] D.F. Hill, K.V. Sharp, R.J. Adrian, Stereoscopic particle image velocimetry measurements of the flow around a Rushton turbine, Experiments in Fluids 29 (5) (2000) 478–485.

[17] A.B. Metzner, R.E. Otto, Agitation of non-Newtonian fluids, AIChE Journal 3 (1) (1957) 3–10.

[18] I. Seyssiecq, A. Tolofoudyé, H. Desplanches, Y. Gaston-Bonhomme, Viscoelastic liquids in stirred vessels - Part I: power consumption in unaerated vessels, Chemical Engineering & Technology 26 (11) (2003) 1155–1165.

[19] Y. Bouremel, M. Yianneskis, A. Ducci, Three-Dimensional deformation dynamics of trailing vortex structures in a stirred vessel, Industrial & Engineering Chemistry Research 48 (17) (2009) 8148–8158.

[20] A. Karnis, S.G. Mason, Particle motions in sheared suspensions. XIX. Viscoelastic media, Transactions of the Society of Rheology 10 (2) (1966) 571–592.

[21] B.M. Lormand, R.J. Phillips, Sphere migration in oscillatory Couette flow of a viscoelastic fluid, The Journal of Rheology 48 (3) (2004) 551–570.

[22] E.F. Lee, D.L. Koch, Y.L. Joo, Cross-stream forces and velocities of fixed and freely suspended particles in viscoelastic Poiseuille flow: perturbation and numerical analyses, The Journal of Non-Newtonian Fluid Mechanics 165 (19–20) (2010) 1309–1327.

[23] G. D'Avino, P.L. Maffettone, F. Greco, M.A. Hulsen, Viscoelasticity-induced migration of a rigid sphere in confined shear flow, The Journal of Non-Newtonian Fluid Mechanics 165 (2010) 466–474, 9–10.

[24] S. Caserta, G. D'Avino, F. Greco, S. Guido, P.L. Maffettone, Migration of a sphere in a viscoelastic fluid under planar shear flow: experiments and numerical predictions, Soft Matter 7 (3) (2011) 1100–1106.

[25] G. D'Avino, et al., Migration of a sphere suspended in viscoelastic liquids in Couette flow: experiments and simulations, Rheologica Acta 51 (3) (Mar. 2012) 215–234.

[26] C.W. Macosko, Rheology: Principles, Measurements, and Applications, Wiley VCH Imprint, 1994. Place of publication not identified.